Simulation and Experimental Characterisation of a 3D-Printed Electromagnetic Vibration Sensor

John Masangkay, Nuwan Munasinghe, Peter Watterson and Gavin Paul

University of Technology Sydney, Australia

ARTICLE INFO

ABSTRACT

Additive manufacturing, also known as 3D printing has already transformed from a rapid prototyping tool to a final end-product manufacturing technique. 3D printing can be used to develop various types of sensors. This paper investigates the ability to use the electromagnetic induction properties of 3D printed carbon-based filament for developing sensors. The paper presents a novel prototype vibration sensor which is 3D-printable, except for an included NdFeB magnet. Motion is detected from the voltage induced by the relative motion of the magnet. The devised vibration sensor is simulated using ANSYS, and a novel prototype is 3D-printed for physical testing to characterise and understand its electromagnetic properties. Simulation helped establish constraints for the design. Two types of experimental setups were physically tested, one setup with a magnet freely sliding inside a cylindrical cavity within an oscillating coil, and the other setup with a stationary coil and oscillating magnet. At a frequency of 10 Hz and a motion travel of about 12 mm, the induced voltage for the moving coil case varied from 5.4 mV RMS for pure sliding motion of the internal magnet to 22.1 mV RMS. The findings of this paper suggest that future sensors can be developed using the electromagnetic induction properties of the carbon-based filament.

1. Introduction

Advanced manufacturing can be defined as technologies, systems and processes that will be used to transform current manufacturing by adding value to the entire supply chain [1]. Additive manufacturing (AM), generally known as 3D printing, is a shaping process that builds 3D geometries using the layer-by-layer addition of material [2]. AM has been applied in advanced manufacturing applications to reduce capital costs, and allowed advanced business models such as customer-led design processes and just-in-time manufacturing [1]. AM has already transformed from a rapid prototyping tool to a final end-product manufacturing technique [3]. Therefore, many different industries, such as medical and construction, have already started to apply this technology [4, 5, 6].

The motivation for the research explained in this paper came from a project where the authors are applying AM for the manufacture of mining equipment called a Gravity Separation Spiral (GSS). The shape profile of the spirals allows a GSS to separate minerals from slurry according to the constituent materials' specific gravities. Customisation is required so bespoke spirals can be easily created for each customer's slurry and separation needs. However, the traditional mould-based manufacturing shown in Fig. 1a does not allow for customisation, due to the inefficiency and cost of having unique single-use moulds. The UTS Rapido team has developed a one-third scale printer (Fig. 1b) and has designed and is developing the full-scale printer, which includes two industrial robot arms with two extrusion nozzles as shown in Fig. 1c [7]. Objects are sliced radially [8], and the optimal robot paths are planned [9] so the extrusion printing expands outwards in a radial arc.

Apart from developing the 3D printer, research is concurrently being conducted on various types of sensors that can be printed inline, embedded inside or mounted outside to remotely monitor the GSS operating conditions [10]. This has led to the development of 3D-printable wear [11], temperature [12], strain sensors [13, 14], and a partial pipe flow meter [15] that can be externally mounted. In this paper, the authors investigated the possibility of developing a 3D printed vibration sensor similar to the other developed sensors. Vibration in equipment can often indicate a problem, or if left unchecked, can cause expedited deterioration [16]. The objective of this research is to investigate and test a novel 3D-printable vibration sensor that can measure the vibration in equipment, such as GSS.

To monitor vibration, Fibre Bragg Grating (FBG) technology is frequently used because of its smaller size, anti-electromagnetic interference, light weight, and corrosion resistance [17, 18]. FBG vibration sensors can be produced through two different techniques - pasting the FBG on the surface [19], or embedding the FBG in elastic material [20]. Wei et al. [21] theoretically analysed a miniaturised FBG vibration sensor and determined its structural parameters by simulation analysis. The size of this sensor was 27 mm x 11 mm x 22 mm with a mass of 5 g. Experimental results showed that the sensor has a sensitivity of 12 pm/g (picometre per gram) in the range of 0-800 Hz, making it suitable for mechanical vibrations in the mid-high frequency range. Igrec et al. [22] developed a 3D printed optic vibration sen-
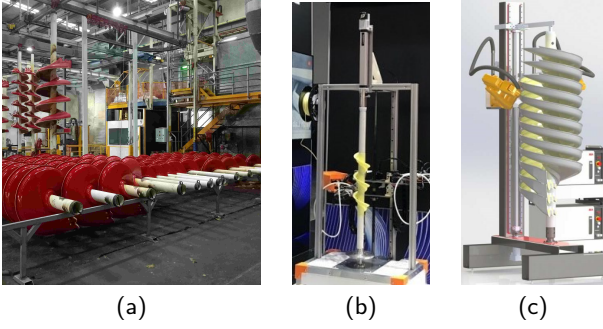
Figure 1: a) A GSS manufacturing facility; b) developed one-third scale printer; c) design of the full-scale printer.

sor based on modulating light intensity with a blade attached to a bendable layer. This sensor showed a linear response for a bandwidth of 10-150 Hz. However, embedding external FBG sensors to a 3D printed object requires pausing the print and placing them or placing them after the print is completed. This requires additional steps. This is one reason that motivated this research to 3D print a vibration sensor.

A flexible piezoelectric vibration sensor based on inter-digitated electrodes printed on polymer-coated paper using graphene nanoparticles was developed by Sinar et al. [23]. The sensor was created through an inkjet printing technique and measures the impact force. From the experiments they have conducted, a repetitive 6.3 N impact force in the frequency range of 1-2.37 Hz generated up to 541 mV$_{\text{p-p}}$. Also, low-amplitude vibrations in the range of 50 Hz to 2.5 kHz generated a voltage output from 25 mV$_{\text{p-p}}$ to 452 mV$_{\text{p-p}}$. Kawa et al. [24] developed an inkjet 3D printed vibration power microgenerator that can generate power in the mW range. The device used a pre-manufactured surface mount inductor (SMD) coil and its design relies on the electromagnetic induction between a coil and a vibrating magnet suspended on 3D printed micro springs. The resulting device has a resonant frequency of 250 Hz. The 3D printer under development is an extrusion-based printer and therefore, these inkjet-printed sensors cannot be used.

Zhang et al. developed prototype 3D-printed smart eye-glasses with embedded Electromyography (EMG) and vibration sensors [25], which have been used to distinguish the signals from chewing different food types for dietary monitoring. The attached vibration sensor which was embedded inside the 3D-printed frame is a commercially available conventional sensor (Model 352C22, PCB Piezotronis, USA). From the experiments, they were able to determine that skull vibrations were immune to ambient noise, and that the EMG did not yield any results from coughing or head movements. Even though this has a 3D printed frame, the actual embedded sensor is a conventional sensor.

Wu et al. developed a skin-inspired tactile sensor for a prosthetic arm based on giant magnetoimpedance material embedded with an air gap [26]. The sensor exhibited a low detection limit of 10 μN. Integrating this tactile sensor with an inductance-capacitance oscillation circuit allowed direct

transduction of force stimuli into digital-frequency signal. A potential application area for this sensor is smart prosthetics, that can functionally replace natural limbs. Because of the special type of material used and the small size, it is not possible to 3D print this sensor.

A vibration energy harvester based on printed polymer multilayers was developed by Godard et al. [27], with the ability to generate around 1 mW from vibration. They used a stack of 10 thin layers of piezoelectric polymer printed on a polymer substrate, and showed that it can then generate up to 0.97 mW at 33 Hz in an area around 2.4 cm^2. An electromagnetic energy harvesting device from vibrations based on permanent magnets has been developed by Yang et al. [28]. The device has resonant frequencies of 369 Hz, 938 Hz and 1184 Hz. For the first and second vibration modes, the observed power output was 0.6 μW and 3.2 μW for an amplitude of 14 μm with a 0.4 mm gap. Another magnet array-based energy harvester was developed by Zhang et al. [29] with the ability to generate around 0.25 W output in submillimeter vibration amplitude. It was able to generate 263 mW power output when it was subjected to 65 Hz. Similar to these different types of energy harvesters that use permanent magnets, the presented 3D printed sensor in this paper also uses a permanent magnet.

Sensors found in the literature are either printed with a different type of printing method compared to the developed printer, developed with non-printable material or sensors are conventional sensors embedded in 3D printed material. Therefore, this paper presents the simulation and testing of a novel 3D-printed vibration sensor based on electromagnetic induction. The sensor includes a coil that is printed in carbon conductive filament and an oscillating permanent magnet located inside the coil. The device was printed using an extrusion-based 3D printer (MakerBot Replicator) and tested using a MB Electronics vibration exciter.

The remainder of the paper is organised as follows. Firstly, Section 2 provides a theoretical background and details of the materials. Section 3 provides the results of the simulation and experiment. Section 4 provides a discussion about the results and finally, Section 5 concludes the paper.

2. Methodology

2.1. Theoretical Basis of the Sensor: Electromagnetic Induction

This section explains how the magnetic flux density, related to induced voltage, can be mathematically represented according to the arrangement of the coil and the movement of the magnet conducted in the experiment.

By Faraday's law for motional emf [30], for a rigid coil moving at velocity, **v**, within a stationary magnetic flux density vector field, **B**, the voltage (or emf), ε, sensed by the coil is given by the line integral along the coil path of the electric field, **E**$'$, in the moving coordinate system of the coil as shown in Eqs. (1)-(2).

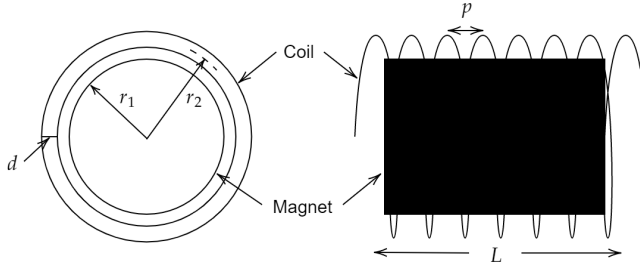$$\varepsilon = \int \mathbf{E}' \cdot d\mathbf{l}. \tag{1}$$

Figure 2: Simplified diagram of the sensor electromagnetic components.

$$\varepsilon = \int (\mathbf{v} \times \mathbf{B}) \cdot d\mathbf{l}. \tag{2}$$

Suppose the vibration sensor has a cylindrical geometry and the sensor housing is attached to some heavy industrial equipment being monitored, and that the housing is made to oscillate sinusoidally along its cylindrical axis with amplitude, A, and angular frequency, ω, as in Eq. (3).

$$x_h = A\cos(\omega t). \tag{3}$$

The magnet located inside the housing cavity may then acquire an axial displacement, x_m, through friction with the housing or through spring suspension. The relative motion of the coil in the axial direction, $\hat{\mathbf{x}}$, is then represented by Eq. (4).

$$\mathbf{v} = v\hat{\mathbf{x}} = (\dot{x}_h - \dot{x}_m)\hat{\mathbf{x}}. \tag{4}$$

For the coaxial, cylindrical, axially magnetised magnet in this application, the flux density in cylindrical coordinates (ρ, φ, x) is $\mathbf{B} = (B_\rho, 0, B_x)$ and $\mathbf{v} \times \mathbf{B} = (0, vB_\rho, 0)$.

2.2. Design of the Sensor

The sensor was designed to be printed using two filaments and can be divided into three parts. The first part is an off-the-shelf neodymium magnet, located inside the sensor assembly. The second part is the coil which has been created using a filament consisting of a mix of carbon and Polylactic Acid (PLA), featuring screw terminals to connect the wires for testing as shown in Fig. 3. This is slotted on the outside of the third part, which is the casing. This coil does not move relative to the case when subjected to vibration. The entire casing design has been created using standard PLA filament and is split into two sections. The first section is attached to the vibrating object, here the vibration exciter. The second section slides and locks into slots in the first section, similar to how a bayonet cap light bulb is twisted into a socket.

As detailed, the sensor works by electromagnetic induction. The idea is for the entire sensor casing to be mounted onto a machine where, if vibration forces are present, the casing moves with the vibrating machine whilst the magnet remains stationary relative to the casing. The physical testing highlighted in the following sections further detail the operation principle of the sensor in action - with the Type
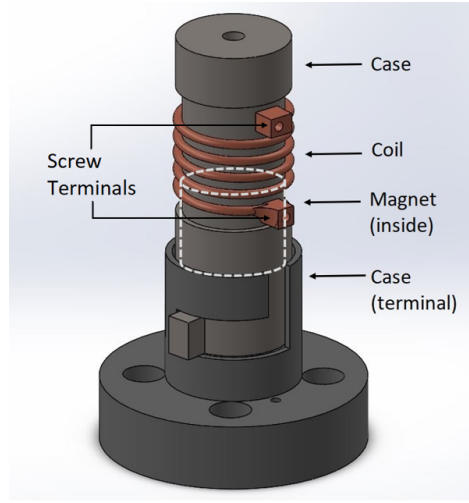

Figure 3: 3D model of the sensor.

2 test providing the ideal scenario where the magnet is suspended, and the Type 1 test where the casing is fixed and the magnet can slide freely inside the cavity.

3. Experimental Results

Before developing the physical sensor, a simulation was conducted with realistic parameters based on the actual sensor design and the results were analysed. The goal of the simulation is to predict whether the resulting signals will be measurable in reality and to build an understanding of the relationship between different parameters and induced voltage. After the simulations demonstrated the relationship between the parameters and induced voltages, the real sensor was printed with similar parameters and tested. Finally, the comparative results of the simulation modelling and the real-world experiments are presented.

3.1. Simulation Setup

Simulations were conducted in ANSYS Maxwell from the ANSYS Electromagnetics Desktop Suite 2019. The focus of the setup were the two main parts of the sensor design, which were the coil and the magnet. A simplified diagram of the simulation model is shown in Fig. 2. In the ANSYS model, the magnet is coaxial with the coil and a linear motion along the x-axis was the designated path assigned to the magnet, oriented as shown in Fig. 4. The coil endpoints are extended outwards and are connected to the ends of a set "region" encasing the entire setup in the shape of a rectangular prism with dimensions 80 mm x 80 mm x 130 mm. This model boundary is identified as air with dimensions four times larger than the magnet diameter and is shown in Fig. 4. The ANSYS model requires the endpoints of the coil to touch the end of the region to assign a current, hence the reason for extending the coil endpoints by 40 mm in the positive and negative z-axis. As the ANSYS simulation model was transient, data was recorded by ANSYS every 0.01 seconds.
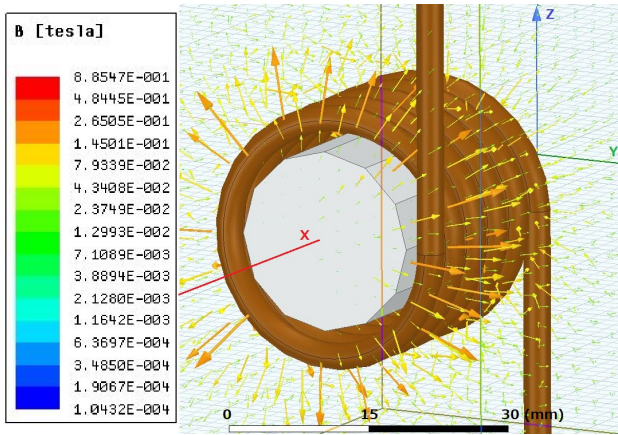
B [tesla]

8.8547E-001
4.8445E-001
2.6505E-001
1.4501E-001
7.9339E-002
4.3408E-002
2.3749E-002
1.2993E-002
7.1089E-003
3.8894E-003
2.1280E-003
1.1642E-003
6.3697E-004
3.4850E-004
1.9067E-004
1.0432E-004

0   15   30 (mm)

Figure 4: Simulated magnetic field (5-turn coil).

In the magnet's initial position, as shown in Fig. 3, the distance between the midpoint of the magnet and the midpoint of the coil is around 15 mm. The coil is stationary and the magnet moves along the x-axis as shown in Fig. 4 and returns back to the same initial position after travelling a one complete cycle around $\sim$75 mm. There were two independent parameters changed within the ANSYS simulation model - the velocity of the magnet, and the number of coil turns. For the first test, two different velocities were simulated, 250 mm/s and 500 mm/s. The second test was conducted at 500 mm/s for all tests, changing the number of coil turns by adding 2 turns at each iteration, starting from 1 turn and increasing up to 7 turns. The ANSYS simulation model parameters are shown in Table 1.

3.2. Simulation Results

The results of the simulation can be observed from Fig. 5 and 6. Fig. 5 shows the voltage induced against time for 5 turns for the two speeds tested. The highest values recorded were when the magnet had travel around 15 mm to be in the middle of the coil: 22 mV for 500 mm/s, and 11 mV for 250 mm/s. Then the voltage starts to drop when the magnet leaves the coil. When the magnet comes back, the voltage (negative) again reaches a maximum absolute value at the same middle point. Finally, the magnet stops at the initial
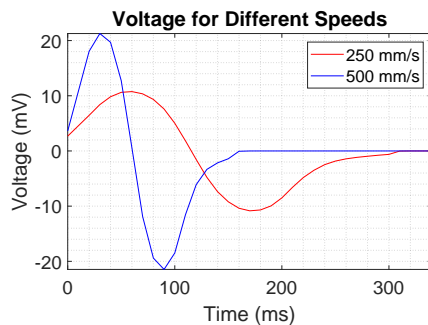

Figure 5: Voltage vs time for 5 turns at different speeds.

Table 1
Simulation parameters

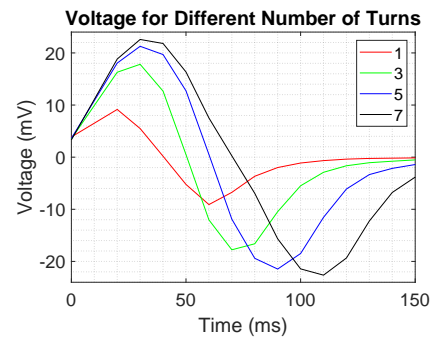| Parameter	Value
Magnet type	Neodymium (N35)
Magnet remanence	1.23 T
Magnet relative permeability	1.045
Coil bulk conductivity	625000 S/m
Magnet diameter ($2r_1$)	20 mm
Magnet axial length (l)	20 mm
Conductor diameter (d)	3 mm
Coil mid diameter ($2r_2$)	26 mm
Coil pitch (p)	5 mm
Magnet cycle travel distance	$\sim$75 mm

Figure 6: Simulated voltage vs time for 500 mm/s and different numbers of turns.

position. The induced voltage is directly proportional to the velocity with an inversely proportional time scale as evident in Fig. 5. The voltage is generated from the time derivative of the linked flux versus the magnet position $\psi(x)$.

For the second simulation, the voltage is plotted for different numbers of turns in Fig. 6. It can be seen that the maximum voltage value was exhibited by the 7-turn coil at 23 mV, and the lowest value from the single-turn coil at about 9 mV. It is evident that the induced voltage increased with the number of turns, but the voltage per turn reduced due to the coil's spatial extent, with only turns near the magnet end face experiencing the peak B_ρ.

From these simulation results, it is evident that the expected induced voltages will be measurable. Additionally, it was possible to understand how the induced voltage patterns change with different parameter sets. These simulation results are henceforth compared with the experimental results from the printed sensor, to see how well the mathematical model matches reality.

3.3. Fabrication of the Sensor

The sensor was printed using the Makerbot Replicator 5th Generation, a single filament commercial 3D printer. The coil was printed individually by utilising breakaway supports and orienting the part to print vertically as shown in Fig. 7a. The print parameters used are listed in Table 2. The limitation of a single filament printer coupled with the complex coil shape meant that each coil turn contained breakaway
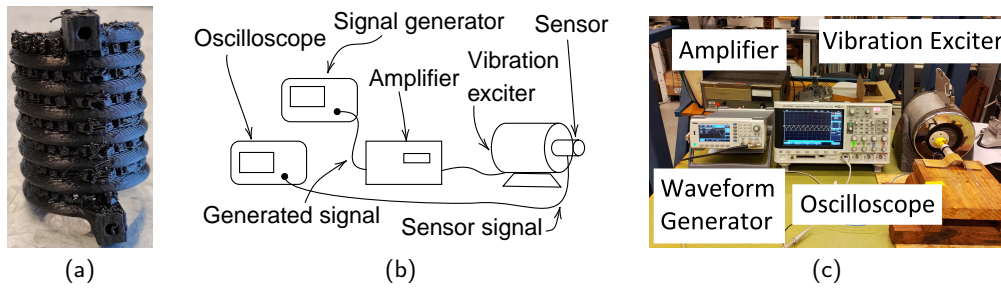
Figure 7: a) Printed coil with supports; b) components of the experiment; c) experimental setup.

Table 2
Print parameters

Parameter	Value
Nozzle diameter	0.4 mm
Bed temperature	60 °C
Nozzle temperature for PLA	215 °C
Nozzle temperature for conductive PLA	215 °C
Printing speed PLA	90 mm/s
Printing speed conductive PLA	20 mm/s

Table 3
Experiment parameters

Parameter	Value
Conductor diameter (d)	3 mm
Coil mid diameter ($2r_2$)	26 mm
Coil pitch (p)	5 mm
Coil bulk conductivity	16.1 S/m
Number of turns (N)	5
Magnet type	Neodymium (N40)
Magnet remanence	1.18-1.25 T
Magnet diameter ($2r_1$)	20 mm
Magnet axial length (l)	20 mm

supports that required manual removal by hand. The trouble with removing the supports in this manner is twofold: it is a time-consuming process; and there is a high risk of breaking or chipping the part during extraction due to its shape. The casing has been printed using standard PLA filament and the coil has been printed using conductive carbon and PLA filament. The overall sensor was assembled by hand after printing multiple components. The aforementioned risks and challenges of assembling the sensor by hand can be solved by printing through a multi-filament printer. A multi-filament printer will ensure precision and shape integrity as the coil will be embedded into the casing during the printing process. This effectively eliminates the need for breakaway supports and coil-to-case assembly.

3.4. Experiment Setup

The general setup for the vibration test consists of five parts - the amplifier, waveform generator, oscilloscope, vibration exciter, and the specimen as shown in Fig. 7b and c. The amplifier supplies the voltage needed to operate the vibration exciter. The waveform generator is connected to the

Figure 8: a) Moving coil with magnet setup; b) stationary coil setup.

amplifier and controls the frequency and amplitude of the exciter, while the oscilloscope records the signal generated by the specimen. The specimen is mounted on the exciter horizontally as shown in Fig. 8a, with the terminals connected to the oscilloscope for data recording. The parameters of the specimen can be found in Table 3. The vibration exciter used was the MB Electronics PM50, with the amplifier MB Electronics Model 2250. The waveform generator used was the Tenma 72-3555 Function/Arbitrary Waveform Generator [31]. The oscilloscope model used was the DSO-X 2004A [32] by Keysight Technologies. Two types of experiment were set up as described in the next two sections.

3.4.1. Type 1 Setup: Moving Coil with the Magnet

In the Type 1 tests, the entire specimen, along with the magnet contained inside, is mounted on the vibration exciter as shown in Fig. 8a. The case vibrates together with the exciter due to its rigid attachment by bolts. The magnet is allowed to freely slide in the cavity within the housing. In Type 1 testing the magnet is confined in a closed space with a limited range of motion and for certain amplitudes and frequencies, the magnet rebounds against the "walls" at the ends of the specimen. Because of this rebound action, irregular vibrations were observed and therefore, the maximum and minimum RMS values were measured in Type 1 testing to increase the reliability of the measurements, and to provide a broader picture rather than providing a single value. However, this was not a problem in Type 2 testing since measurements are stable for a given frequency and there were no significant differences when measuring the maximum or minimum. Therefore, in the Type 2 test, only a single output
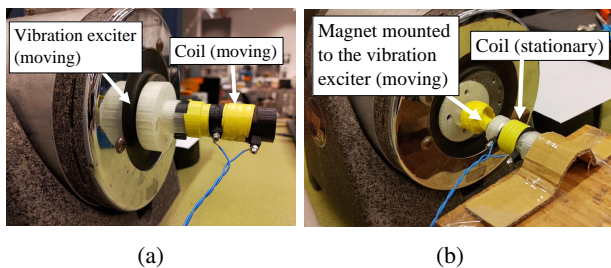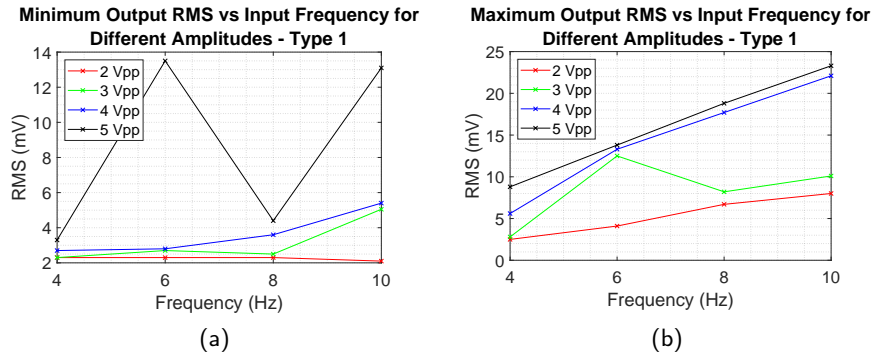
Figure 9: Moving coil (Type 1) results for maximum magnet internal travel of 30 mm: a) min RMS; b) max RMS.

RMS value is shown (Fig. 11b). The magnet is able to move a maximum distance of 30 mm within the cavity relative to the housing.

3.4.2. Type 2 Setup: Stationary Coil and Moving Magnet

Type 2 tests involved a moving magnet with an open-ended stationary coil fixed in space as shown in Fig. 8b. Thus, only the magnet was mounted to the exciter, with a non-magnetic clamp holding the coil at a distance just before the magnet face enters the coil, where the maximum voltage can be measured. This second test was conducted on the same vibration exciter under the same conditions as the Type 1 tests to remove the uncertainty associated with the magnet motion.

3.5. Type 1 Results: Moving Coil Along With the Magnet

Two variables were tested in the first experiment: frequency, and amplifier input amplitude. The output RMS voltage generated was observed directly from the oscilloscope reading shown on the screen for a set of amplifier input amplitudes and frequencies. Adjustments were made at the waveform generator. The amplifier amplification factor was set at 5 out of 10. As the peak-to-peak voltage can potentially fluctuate due to extreme values in the Type 1 test, the maximum and minimum RMS voltage was instead measured to increase the reliability of the measurements. This was achieved by letting the specimen oscillate for 20 seconds and recording the highest and lowest RMS voltages over any 2-second period within the 20 second duration. Using this method the maximum and minimum RMS values were measured. The amplitude was raised from 2 Volts peak-to-peak (V_{pp}) in increments of 1 V_{pp} up to 5 V_{pp}. At each of the amplitude steps, the frequency was varied, initially set at 4 Hz, then raised in increments of 2 Hz up to 10 Hz. The results of the tests can be seen in Fig. 9.

It is important to note that results in the 5 V_{pp} range cause the amplifier to "overcurrent" and in turn skew the results. Hence, only measurements up to the 4 V_{pp} range will be considered. From the graphs, it is shown that the highest generated voltage was achieved by the highest frequency (10 Hz) and amplitude (4 V_{pp}), at a maximum of

22.1 mV RMS (Fig. 9b) and a minimum of 5.4 mV RMS (Fig. 9a). The lowest voltage range recorded was at the lowest frequency (4 Hz) and amplitude (2 V_{pp}) setting tested, where the RMS was between a maximum of 2.5 mV and a minimum of 2.3 mV RMS. Comparing the maximum and minimum graphs shows the erratic behaviour of the magnet. For example, as previously stated at 10 Hz and 4 V_{pp}, the maximum induced voltage recorded was 22.1 mV RMS, whilst the minimum was 5.4 mV RMS, differing by a factor of approximately 4. At this frequency and amplitude, the magnet rebounding off the cavity walls introduces harmonics that cause short bursts of oscillation at a higher or lower frequency, providing a large difference between the minimum and maximum induced voltages, thus resulting in an inconsistent voltage induction. This rebound effect only occurred in few scenarios. However, it is planned to develop a mechanism to mitigate this in future.

3.6. Type 2 Results: Moving Magnet With Stationary Coil

The Type 2 test was conducted for the same device components but with the magnet fixed to the vibration exciter and moving within an open-ended case for unobstructed oscillation. Additionally, to the same variables tested in Section 3.5, which are frequency and amplifier input amplitude, the number of coil turns was also changed to understand the effect. The initial amplitude was the same as the Type 1 setup, 2 V_{pp}, increasing in increments of 1 V_{pp}, to 5 V_{pp}, with the frequencies increasing from 4 Hz to 10 Hz in 2 Hz steps. The amplifier amplification factor was set at 5 out of 10.

Due to the amplitude being measured in peak-to-peak voltage, a test has also been conducted to translate the relationship between that amplitude and the travel, i.e. the moving distance, of the vibration exciter. A slow-motion camera (240 fps) was set up facing the side of the vibration exciter, with a non-steel ruler placed alongside the housing. The measured travel distances (tolerance ± 1 *mm*) are shown for 10 Hz in Fig. 10a. The graph shows a near-linear relationship between the travel distance versus the amplifier input amplitude.

A comparison of videos for 5 Hz and 10 Hz indicated that the travel was approximately independent (within a tol-
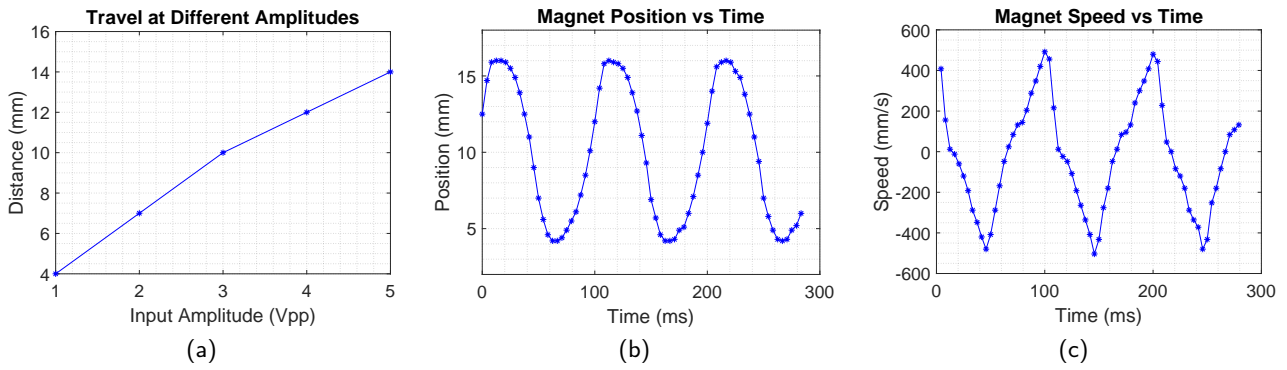
Figure 10: Moving magnet tests (Type 2): a) travel distance of the vibration exciter vs input amplitude for 10 Hz; b) exciter position versus time for 4 V_{pp} with s 10 Hz excitation and 12 mm travel distance; c) speed vs time of the exciter.
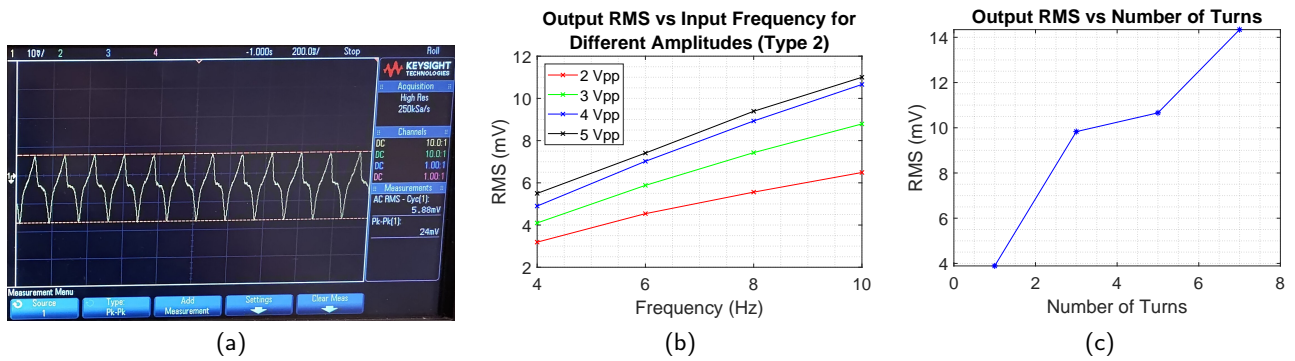

Figure 11: Moving magnet (Type 2) results: a) sample signal received from sensor in oscilloscope at 6 Hz and 3 V_{pp}; b) output signal RMS for different input frequencies for 5 turns; c) output signal RMS for different numbers of turns at 10 Hz and 4 V_{pp}.

erance) of the frequency, for the given V_{pp}. Fig. 10b and c plot the position and calculated velocity versus time for the moving magnet (Type 2) 4 V_{pp} and 10 Hz test, travel approximately 12 mm, indicating that although it is cyclical, the exciter motion deviates from the expected perfect sinusoidal shape.

The sample coil voltage waveform (Fig. 11a) exhibits features similar to the velocity waveform (Fig. 10c), indicating that the non-sinusoidal exciter velocity profile has contributed to harmonics in the voltage waveform.

In Fig. 11b, we can see that the highest voltage (RMS) recorded was 10.66 mV, from an amplitude of 4 V_{pp} at a frequency of 10 Hz, with the lowest at 2 V_{pp} at a frequency of 4 Hz, generating 3.19 mV. The coil turn test is conducted at an amplitude of 4 V_{pp} at 10 Hz for 1, 3, 5, and 7 coil turns. The results are shown in Fig. 11c, where an increase in the number of turns led to an increase in the voltage induced. One coil turn generated 3.89 mV (RMS), increasing to 9.83, 10.66, and 14.34 mV for 3, 5, and 7 coil turns, respectively.

4. Discussion

The aim of this experiment is to understand the electromagnetic induction behaviour of 3D printed filaments and develop a simple prototype vibration sensor. Considerable research has been conducted on printed vibration sen-

sors, but most rely on complex materials such as graphene nanoparticles [23], or special techniques such as Fibre Bragg Brating (FBG) [17, 18], or inkjet 3D printing [24]. Here, a simpler prototype design has been developed that allows for the analysis of electromagnetic induction in commercially available conductive filaments. An initial simulation has been performed through ANSYS model to get an understanding of the relationship between parameters of the general design such as velocity and number of turns, hence, creating the foundation for the design developed for physical testing.

The Type 2 test simulates an ideal scenario where there is zero friction between the magnet and the coil, and the magnet is suspended whilst the coil oscillates. The Type 1

Table 4

Comparison of ANSYS simulation and experimental results (mV RMS) for moving magnet tests (Type 2) for 4 Vpp input amplitude, 5 turns.

Freq. (Hz)	Pred. (mV)	Meas. (mV)	Pred./Meas.
4	4.69	4.9	0.96
6	7.04	7.02	1.00
8	9.38	8.93	1.05
10	11.73	10.66	1.10

test attempts to simulate a more real-world scenario where it mimics the purpose of the sensor (that is, to be attached to a vibrating machine), meaning that both the coil and the magnet will experience the oscillating force. Although it is important to note that in the Type 1 test, the substantial frictional force that is present moved the magnet, causing it to eventually rebound against the casing walls. Ideally, a suspension mechanism needs to be implemented to achieve complete isolation from the relative moving forces.

The two experiment models generated significantly different results. During Type 1 tests, at the highest frequency (10 Hz) and amplitude (4 V_{pp}), the recorded maximum RMS value was 22.1 mV (Fig. 9b) and the minimum RMS value was 5.4 mV (Fig. 9a). For Type 2 tests, the highest voltage (RMS) recorded was 10.66 mV, from an amplitude of 4 V_{pp} at a frequency of 10 Hz. The Type 1 model has proved capable of voltage induction (RMS). However, occasional irregular vibration was observed inside the specimen, which caused different results. This irregular vibration is believed to be due to rebound when the magnet hits flat walls (i.e. base or top) of the cylindrical casing. The Type 2 test with the magnet moving within a stationary coil has no such vibration. In all experiments, as the number of turns increased, the amount of induced voltage was also observed to increase.

By comparing the maximum induced voltage between the two experiment types it can be seen that the first setup exhibited an overall higher voltage induction. The measurement of both the minimum and maximum RMS voltages is able to overcome situations where the induction is sometimes unreliable. The graph in Fig. 9a shows that the minimum RMS voltage can be as low as 2 mV. Comparing the corresponding amplitude and frequency to the maximum induced voltage in Fig. 9b indicated that the jump can be as big as 17 mV within the same conditions. Furthermore, as this occurs in short bursts, simply averaging the results between the minimum and maximum would prove inaccurate. The minimum RMS voltage for 10 Hz and 4 V_{pp} was 5.4 mV RMS for the moving coil test (Type 1), half that of the 10.66 mV RMS for the moving magnet test (Type 2). The voltage is lower in the moving coil tests because the motion of the magnet induced by friction (surface roughness of PLA ~65.19 μm [33]) reduces the relative motion of the coil and magnet, **v** in Eq. (4). Future work will be conducted to develop a suspension mechanism to eliminate this effect.

The objective of the initial simulation was to determine if the induced voltages are within measurable range and to understand the patterns of these induced voltages. The actual vibration exciter in the experiment seems to have a near-sinusoidal velocity profile (Fig. 10a). However, the finite element analysis can be used to predict the RMS voltage of the Type 2 experiments as follows. The motion is approximated as a sinusoidal function. Given a maximum travel of 12 mm at 10 Hz for 4 V_{pp}, $A = 6\ mm$ and $\omega = 62.83\ rad/s$ in Eq. (3) and the maximum magnet velocity would be $\omega A = 377\ mm/s$. From Fig. 6, the predicted amplitude of the sinusoidal voltage for a 5-turn coil, when positioned to obtain the maximum voltage, is $(377/500) \times 22\ mV = 16.59\ mV$.

The ϵ waveform is not sinusoidal even for the sinusoidal motion because the ϵ for the given speed falls away from the peak (Fig. 5). Thus, the RMS would be somewhat lower than $1/\sqrt{2}$ times the amplitude, 11.73 mV. From Fig. 11b, the measured RMS voltage in the moving magnet test (Type 2) was 10.66 mV, which is 10% lower than the prediction. Using this method with the same travel of 12 mm and applying different frequencies, the voltages at 4, 6, and 8 Hz at 4 V_{pp} have also been predicted and are shown in Table 4. Thus, the actual results closely match with simulations.

The main objective of this research is to understand the ability to use 3D printed conductive materials for sensors that relies on electromagnetic induction. From these tests, it was possible to understand the behaviour of electromagnetic induction in a 3D printed material created from a commercially available conductive filament, by using a simple model of a vibration sensor. Compared to different methods found in the literature as mentioned in Section 1, this proposed method is novel since it reduces the manufacturing cost by using commercially available material and printers to develop the sensor. Since this research proves the ability to use such material for electromagnetic induction based 3D printed sensors, this paper contributes to the area of 3D printed sensor development by enabling the possibility of using 3D printed conductive material in different electromagnetism-based sensors. In future, the use of linear bearing arrangements such as helical springs will be investigated in order to eliminate the irregular vibration.

5. Conclusion

This research has characterised the electromagnetic properties of a novel 3D printed vibration sensor using a commercially available carbon-based conductive filament. Computer simulation has helped ascertain and establish constraints in the design, as well as provide information on the relationship between several parameters. Physical testing has provided an in-depth understanding of the electromagnetic capabilities of the material and prototype. Results have shown that the current design with a moving coil and sliding magnet is capable of voltage induction up to 22 mV. The findings of this paper suggest that future sensors can be developed based on the electromagnetic induction properties of the carbon-based filament. Future work will be conducted to make the sensor more robust by increasing the strength and durability of the housing design, and eliminating the high-frequency vibration that can occur in certain scenarios.

6. Acknowledgement

References

[1] CSIRO, "Advanced manufacturing : A Roadmap for unlocking future growth opporunities for Australia," Tech. Rep. November, 2016.

[2] ISO;ASTM, "ASTM52900 Standard Terminology for Additive Manufacturing," Tech. Rep., 2015.

[3] K. V. Wong and A. Hernandez, "A Review of Additive Manufacturing," *ISRN Mechanical Engineering*, vol. 2012, no. 208760, p. 10, 2012.

[4] G. Z. Cheng, E. Folch, A. Wilson, R. Brik, N. Garcia, R. S. J. Estepar, J. O. Onieva, S. Gangadharan, and A. Majid, "3D Printing and Personalized Airway Stents," *Pulmonary Therapy*, vol. 3, no. 1, pp. 59–66, 2017.

[5] P. Shakor, S. Nejadi, G. Paul, and S. Malek, "Review of Emerging Additive Manufacturing Technologies in 3D Printing of Cementitious Materials in the Construction Industry," *Frontiers in Built Environment*, vol. 4, 2019.

[6] D. D. Camacho, P. Clayton, W. O'Brien, R. Ferron, M. Juenger, S. Salamone, and C. Seepersad, "Applications of Additive Manufacturing in the Construction Industry," in *Automation in construction*, vol. 34, Vilnius, 2017, pp. 1–8.

[7] Engineers Australia, "Milestone for mining manufacture with 3D printing," 2019. [Online]. Available: https://portal.engineersaustralia.org.au/news/milestone-mining-manufacture-3d-printing

[8] N. Munasinghe and G. Paul, "Radial slicing for helical-shaped advanced manufacturing applications," *The International Journal of Advanced Manufacturing Technology*, vol. 112, no. 3-4, pp. 1089–1100, 2020.

[9] ——, "Path Planning for Robot Based Radial Advanced Manufacturing Using Print Space Sampling," in *Int. Conf. on Control, Automation, Robotics and Vision*, 2020.

[10] ——, "Advanced Manufacturing of Spirals for Mineral Separation with Integrated Smart Sensing," in *IEEE UNITE*, 2019. [Online]. Available: http://hdl.handle.net/10453/135218

[11] M. I. N. P. Munasinghe, L. Miles, and G. Paul, "Direct-Write Fabrication of Wear Profiling IoT Sensor for 3D Printed Industrial Equipment," in *Int. Symposium on Automation and Robotics in Construction*, 2019, pp. 862–869.

[12] N. Munasinghe and G. Paul, "Integrated 3-D Printable Temperature Sensor for Advanced Manufacturing," in *Australasian Conference on Robotics and Automation*, 2020.

[13] N. Munasinghe, J. Masangkay, and G. Paul, "Temperature Compensated 3D Printed Strain Sensor for Advanced Manufacturing Applications," in *IEEE Int. Conf. on Robotics and Automation*, 2021.

[14] N. Munasinghe, M. Woods, L. Miles, and G. Paul, "3-D Printed Strain Sensor for Structural Health Monitoring," in *IEEE Int. Conf. on Cybernetics and Intelligent Systems and the Int. Conf. on Robotics, Automation and Mechatronics*, 2019.

[15] N. Munasinghe and G. Paul, "Ultrasonic-Based Sensor Fusion Approach to Measure Flow Rate in Partially Filled Pipes," *IEEE Sensors Journal*, vol. 20, no. 11, pp. 6083–6090, 2020.

[16] S. W. Doebling, C. R. Farrar, and M. B. Prime, "A summary review of vibration-based damage identification methods," *Shock and vibration digest*, vol. 30, no. 2, pp. 91–105, 1998.

[17] R. Di Sante, "Fibre Optic Sensors for Structural Health Monitoring of Aircraft Composite Structures: Recent Advances and Applications," *Sensors*, vol. 15, no. 8, pp. 18 666–18 713, 2015.

[18] P. Antunes, H. Lima, H. Varum, and P. André, "Static and dynamic structural monitoring based on optical fiber sensors," in *Int. Conf. on Transparent Optical Networks*, 2010, pp. 1–4.

[19] M. M. Khan, N. Panwar, and R. Dhawan, "Modified cantilever beam shaped FBG based accelerometer with self temperature compensation," *Sensors and Actuators A: Physical*, vol. 205, pp. 79–85, 2014.

[20] J. Wang, Y. Yu, Y. Chen, H. Luo, and Z. Meng, "Research of a double fiber Bragg gratings vibration sensor with temperature and cross axis insensitive," *Optik*, vol. 126, no. 7, pp. 749–753, 2015.

[21] L. Wei, D. Jiang, L. Yu, H. Li, and Z. Liu, "A novel miniaturized fiber bragg grating vibration sensor," *IEEE Sensors Journal*, vol. 19, no. 24, pp. 11 932–11 940, 2019.

[22] B. Igrec, M. Bosiljevac, Z. Sipus, D. Babic, and S. Rudan, "Fiber optic vibration sensor for high-power electric machines realized using 3D printing technology," in *Photonic Instrumentation Engineering III*, vol. 9754, 2016, p. 975410.

[23] D. Sinar and G. K. Knopf, "Disposable piezoelectric vibration sensors with PDMS/ZnO transducers on printed graphene-cellulose electrodes," *Sensors and Actuators A: Physical*, vol. 302, p. 111800, 2020.

[24] B. Kawa, K. Sliwa, R. Walczak, and V. C. Lee, "Inkjet 3D printed vibrational energy harvester," in *Int. Conf. on Micro and Nanotechnology for Power Generation and Energy Conversion Applications*, 2019, pp. 1–4.

[25] R. Zhang and O. Amft, "Bite Glasses - Measuring chewing using EMG and bone vibration in smart eyeglasses," in *ACM Int. Symposium on Wearable Computers*, 2016, pp. 50–52.

[26] Y. Wu, Y. Liu, Y. Zhou, Q. Man, C. Hu, W. Asghar, F. Li, Z. Yu, J. Shang, G. Liu, M. Liao, and R. W. Li, "A skin-inspired tactile sensor for smart prosthetics," *Science Robotics*, vol. 3, no. 22, 2018.

[27] N. Godard, L. Allirol, A. Latour, S. Glinsek, M. Gérard, J. Polesel, F. Domingues Dos Santos, and E. Defay, "1-mW Vibration Energy Harvester Based on a Cantilever with Printed Polymer Multilayers," *Cell Reports Physical Science*, vol. 1, no. 6, p. 100068, 2020.

[28] B. Yang, C. Lee, W. Xiang, J. Xie, J. Han He, R. K. Kotlanka, S. P. Low, and H. Feng, "Electromagnetic energy harvesting from vibrations of multiple frequencies," *Journal of Micromechanics and Microengineering*, vol. 19, no. 3, p. 035001, 2009.

[29] Q. Zhang and E. S. Kim, "Vibration Energy Harvesting Based on Magnet and Coil Arrays for Watt-Level Handheld Power Source," *Proceedings of the IEEE*, vol. 102, no. 11, pp. 1747–1761, 2014.

[30] J. D. Jackson, *Classical Electrodynamics*. New York: John Wiley and Sons Inc, 1962.

[31] TENMA, "Function / Arbitrary Waveform Generator," Tech. Rep., 2018.

[32] Keysight-Technologies, "Keysight InfiniiVision 2000 X-Series Oscilloscopes," Tech. Rep., 2000.

[33] M. S. Alsoufi and A. E. Elsayed, "Surface roughness quality and dimensional accuracy—a comprehensive analysis of 100% infill printed parts fabricated by a personal/desktop cost-effective FDM 3D printer," *Materials Sciences and Applications*, vol. 9, no. 1, pp. 11–40, 2018.